

Fracture energy of high-Poisson's ratio oxide glasses

To, Theany; Gamst, Christian; Østergaard, Martin Bonderup; Jensen, Lars Rosgaard; Smedskjær, Morten Matstrup

Published in:
Journal of Applied Physics

DOI (link to publication from Publisher):
[10.1063/5.0096855](https://doi.org/10.1063/5.0096855)

Creative Commons License
Unspecified

Publication date:
2022

Document Version
Accepted author manuscript, peer reviewed version

[Link to publication from Aalborg University](#)

Citation for published version (APA):
To, T., Gamst, C., Østergaard, M. B., Jensen, L. R., & Smedskjær, M. M. (2022). Fracture energy of high-Poisson's ratio oxide glasses. *Journal of Applied Physics*, 131(24), Article 245105. <https://doi.org/10.1063/5.0096855>

General rights

Copyright and moral rights for the publications made accessible in the public portal are retained by the authors and/or other copyright owners and it is a condition of accessing publications that users recognise and abide by the legal requirements associated with these rights.

- Users may download and print one copy of any publication from the public portal for the purpose of private study or research.
- You may not further distribute the material or use it for any profit-making activity or commercial gain
- You may freely distribute the URL identifying the publication in the public portal -

Take down policy

If you believe that this document breaches copyright please contact us at vbn@aub.aau.dk providing details, and we will remove access to the work immediately and investigate your claim.

Fracture energy of high-Poisson's ratio oxide glasses

Theany To¹, Christian Gamst¹, Martin B. Østergaard¹, Lars R. Jensen², Morten M. Smedskjaer^{1,*}

¹ *Department of Chemistry and Bioscience, Aalborg University, 9220 Aalborg, Denmark*

² *Department of Materials and Production, Aalborg University, 9220 Aalborg, Denmark*

* Corresponding author. E-mail: mos@bio.aau.dk

Abstract

The apparent relationship between Poisson's ratio and fracture energy has been used to guide the discovery of ductile glasses, with a brittle-to-ductile (BTD) transition at Poisson's ratio around 0.32. Most organic and metallic glasses possess Poisson's ratio above 0.32 and thus feature a fracture energy that is around three orders of magnitude higher than that of oxide glasses, which feature Poisson's ratio typically below 0.30. However, whether the BTD transition can also be observed in oxide glasses remains unknown due to the lack of fracture energy measurements on oxide glasses with high Poisson's ratio. In this work, we measure the fracture energy of six oxide glasses with high Poisson's ratio between 0.30 to 0.34. We find no clear relationship between the two parameters even those that possess the same Poisson's ratio as ductile metallic glasses. This suggests that Poisson's ratio is not the main property to enhance the fracture energy of oxide glasses. To this end, we instead find a positive relation between fracture energy and Young's modulus of oxide glasses, and even for some metallic glasses, which could explain their absence of ductility.

1. Introduction

Oxide glasses are ubiquitous in everyday life, from nanofibers in optics to large windows in high-rise buildings. Their interesting properties include high transparency, high hardness, low-cost of raw materials, high chemical durability in many cases, and easy forming and shaping at relatively low temperature. However, the brittleness of oxide glasses is the major hindrance for their possible use in various functional applications [1,2]. The theoretical strength of oxide glasses is estimated to be around a hundred times higher than their practical strength. [3]. The presence of flaws, mostly on the surface, induces stress singularities, and consequently less energy is needed in practice relative to theory to fracture oxide glasses.

Although flaw formation is known as the cause of strength reduction, the crack tip formation and growth mechanisms are not well understood, making it a challenge to design damage-resistant, ductile oxide glasses. Post-processing methods such as chemical strengthening on the glass surface are used to improve the mechanical properties of current commercial oxide glasses [4], and molecular dynamics simulations and nanoscale sample experiments suggest that some oxide glasses such as silicate and aluminate glasses can exhibit some nanoscale ductility [5–8]. More, indentation studies have shown that aluminoborate glass can exhibit some microscale ductility upon aging in room humidity atmosphere based on its very high (~400 N) crack resistance, i.e., resistance to initiate cracks upon indentation [9]. Another study on hot-compressed oxide glasses shows that, in a macroscale specimen experiment, a record-high fracture toughness (~1.4 MPa m⁻¹) can be achieved, which reflects the resistance to crack extension [10]. The increase in fracture toughness is ascribed to the increase of nanoscale ductility upon hot-compression. Interestingly, studies on metals and metallic glasses have shown that low Poisson's ratio favors brittleness [11,12]. This observation is based on a correlation between fracture energy, i.e., the energy required to open a unite area of crack surface, and the Poisson's ratio. Specifically, the Poisson's ratio of about 0.32 represents a brittle-to-ductile (BTD) transition not only for metallic glasses but for a wider range of non-crystalline solids [12,13].

Most oxide glasses exhibit Poisson's ratio below 0.30, making it difficult to test the BTD transition hypothesis for this material family. Although some oxide glasses were reported to have Poisson's ration greater than 0.33 [14,15], their reproduction, measurement, and the difficulty in processing them caused by their highly hydroscopic nature make them unsuitable for the present experiment. In this paper, we synthesize six oxide glasses with high Poisson's ratio from ~0.30 to ~0.34. The glasses are chosen based on

existing high-Poisson's ratio glasses in literature [16–18] and composition modification based on the assumption that high atomic packing density leads to high Poisson's ratio [19]. We determine their fracture energy by using a self-consistent method, namely the single-edge precracked beam (SEPB) method. We also measure the elastic moduli of these glasses to establish a relationship between the elastic moduli and fracture energy. To this end, we discuss the role of Poisson's ratio and Young's modulus on the fracture energy and thus the ductility in oxide glasses.

2. Methods

2.1. Sample preparation

For this study, we selected six different oxide glasses, namely (nominal, in mol%) 20La₂O₃-30Al₂O₃-50B₂O₃ (20La30Al50B), 20La₂O₃-20Al₂O₃-10Ga₂O₃-50B₂O₃ (20La20Al10Ga50B), 15Cs₂O-30BaO-55B₂O₃ (15Cs30Ba55B), 22.5Cs₂O-22.5BaO-55B₂O₃ (22.5Cs22.5Ba55B), 5Cs₂O-50ZnO-45B₂O₃ (5Cs50Zn45B), and 2Ta₂O₅-55ZnO-43B₂O₃ (2Ta55Zn43B). The glasses were chosen because they are estimated to have the Poisson's ratio (ν) greater than 0.30 based on literature and a claim that ν increases with increasing atomic packing density (C_g) [19]. Lanthanum alumino/gallioborate glasses were chosen because 25La₂O₃-15Al₂O₃-60B₂O₃ has $\nu \sim 0.30$ [16], and the increase of Al₂O₃, as well as the replacement of Al₂O₃ by Ga₂O₃, leads to the increase of C_g . Cesium barium-borate glasses were chosen because cesium borate glasses have $\nu > 0.30$ when Cs₂O \geq 15 mol% but are high hygroscopic [18], and the replacement of Cs₂O/B₂O₃ by BaO was done to improve the chemical durability. The zinc-borate glasses were chosen based on Ref. [17].

The glasses were prepared by the traditional melt-quenching technique using commercially chemical powders. We used adequate amounts of La₂O₃ (Sigma Aldrich, purity > 99.9%), Al₂O₃ (Sigma Aldrich, > 99.5%), H₃BO₃ (Honeywell, >99.5%), Ga₂O₃ (Sigma Aldrich, > 99.9%), Cs₂CO₃ (Sigma Aldrich, >99.9%), BaCO₃ (Sigma Aldrich, >99.9%), and ZnO (Sigma Aldrich, >99.9%) powders. These powder mixtures were then added stepwise into a Pt-Rh crucible and melted in an electric furnace (Entech, Ängelholm). According to their viscosity, the 20La30Al50B, 20La20Al10Ga50B, and 2Ta55Zn43B melts were homogenized at 1450 °C for 2.5 h, whereas the 15Cs30Ba55B, 22.5Cs22.5Ba55B and 5Cs50Zn45B melts were homogenized at

1050 °C for 2 h. The homogenized melts were quenched by pouring them onto a brass plate and pressing with a steel plate, followed by annealing at their estimated glass transition temperature (T_g) for 30 min.

The measured T_g was determined by differential scanning calorimetry (DSC, 449C Netzsch). We prepared a disk-shaped sample of diameter of ~5 mm with two polished surfaces to have a height of ~1 mm. The prepared sample was then placed in a Pt crucible and heated up to the estimate $T_g + 70$ °C before cooling down to 100 °C to finish one scan. We did two scans with the same rate of 10 °C min⁻¹ for both heating up and cooling down processes. The T_g was then determined from the second upscan, specifically as the intercept between the extrapolated sub- T_g signal and the tangent of the endothermic glass transition peak. Lastly, we reannealed the glasses at their measured T_g for 30 min.

2.2. Density and elastic moduli

We determined the density (ρ) of each glass by Archimedes principle of buoyancy in absolute ethanol using a specimen of 3×10×25 mm³. Young's modulus (E), shear modulus (G), bulk modulus (K) and Poisson's ratio (ν) were measured by means of ultrasonic echography using the same specimen. For this moduli measurement, we confirmed the coplanar surfaces to be better than 10 μm between 10 mm length, i.e., the slope was less than 0.001, to assure the measuring accuracy. From the measured ρ and thickness (3 mm), we determined the longitudinal and transversal sound wave velocities (V_L and V_T , respectively). To do so, we used 20 MHz delay line transducers that were connected to an ultrasonic thickness gauge (38DL Plus, Olympus). Using Eqs. (1)-(4), we could then calculate the moduli [20].

$$E = \rho \frac{3V_L^2 - 4V_T^2}{(V_L/V_T)^2 - 1}, \quad (1)$$

$$G = \rho V_T^2, \quad (2)$$

$$B = \rho \frac{3V_L^2 - 4V_T^2}{3}, \quad (3)$$

$$\nu = \frac{V_L^2 - 2V_T^2}{2(V_L^2 - V_T^2)}. \quad (4)$$

2.3 Fracture energy

To measure the fracture energy (G_c), we used the single-edge precracked beam (SEPB) method [1,21]. The first step in this method is to cut and polish the sample to a rectangular shape with dimensions of $B \times W \times L$, where B (breadth) varies from 2 to 3 mm, W (width) from 3 to 4 mm, and L (length) from 24 to 30 mm (**Figure 1a**). In any variation, B is smaller than W and follows the proportion as $0.5 \leq B/W \leq 1$ to ensure the plane strain conditions and to ease the precrack production. We then polished the sample, in the final step, with 3 μm diamond paste to remove any surface residual stresses and critical surface flaws. The polished sample was then indented as a line in the center of one B side (**Figure 1a**), by using a Vickers indenter, to guide the creation of the precrack in the bridge-compression fixture (**Figure 1b**). The indented specimen was positioned by ensuring that the indentation line is in the middle of the groove of the bridge-compression fixture. The groove size (b as in **Figure 1b**) is chosen to ensure the b/W ratio of ~ 1.5 to facilitate the creation of a sharp precrack length (a as in **Figure 1c**) with the a/W ratio of ~ 0.5 [21]. During the bridge-compression, the indented specimen experienced compression on the upper part and traction on the lower part, causing the connections of the indents' corner cracks and then growing to around the a/W ratio of ~ 0.5 (i.e., to where the compressive stress exists). The precracked specimen was then positioned into the three-point bending set-up and the load was operated with a displacement rate of $15 \mu\text{m s}^{-1}$ until the specimen was fractured into two pieces (**Figure 1c**). In the bridge-compression and the three-point bending experiments, we applied load using a 100 kN universal testing machine (Z100, Zwick) with load cells of 100 kN and 1 kN, respectively. We note that the use of the load cell of 1 kN or smaller for the three-point bending step is important here, for the reason of precision, since the precracked specimens break mostly when the applied load is below 10 N. The fractured specimen, after the three-point bending test, was then used to measure the fracture surface (as illustrated in **Figure 1d** and described in detail in Ref. [2]). From the three-point bending test, we also measured the load-displacement curves to obtain the work of fracture (wof , see Section 2.4), and together with the fracture surface (A as in **Figure 1e**), we calculated the fracture energy (**Figure 1e-g**).

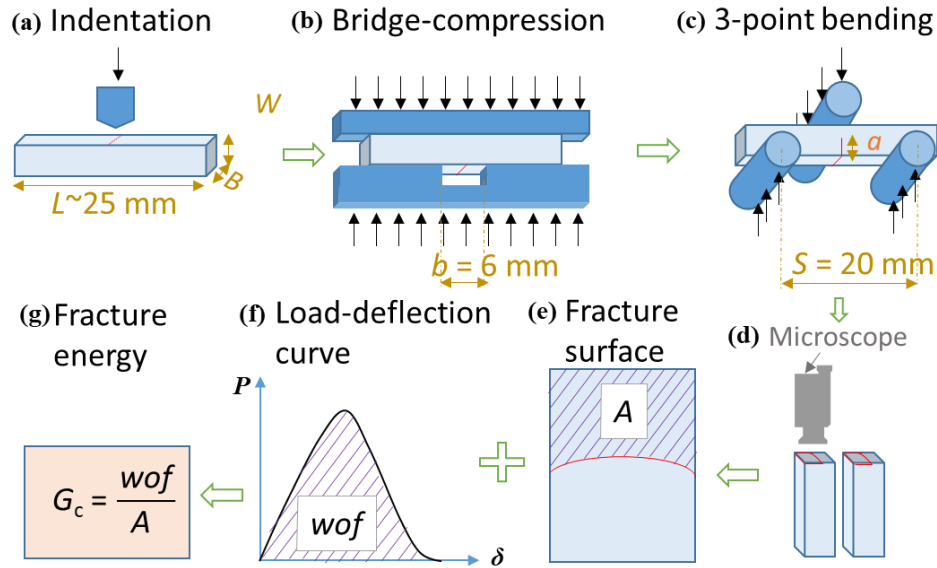


Figure 1: Principle of the single-edge precracked beam (SEPB) method to determine the fracture energy: (a) indentation, (b) bridge-compression, (c) three-point bending, (d) microscopy, (e) fracture surface marked with A, (f) load-deflection (P - δ) curve, and (g) fracture energy (G_c) calculated from work of fracture (wof) and fracture surface (A). Light blue block represents the glass specimen, dark blue block represents the set-up, red line represents the indentation and precrack line, black arrow line represents the applied load, and the golden bi-arrow line represents the dimension.

2.4 Specimen deflection for fracture calculations

To calculate the real wof , we need to know the real specimen deflection [21]. A displacement that we directly obtained from the three-point bending test is the total displacement (δ_t), which is the accumulation of a machine displacement (δ_m) and a specimen deflection (δ_s), i.e. $\delta_t = \delta_m + \delta_s$. It is noteworthy that here δ_m is not equal to only the load cell displacement, but the whole set-up displacement, e.g., the displacement from the load cell, the upper- and lower-rollers of the bending test, the machine actuator, and the support plate below the lower-rollers. Hence, the value δ_m for the set-up used for the three-point bending test needs to be known.

To determine the δ_m , we used an as-polished rectangular beam of a soda-lime-silica glass (SLS, also known as window glass) as a reference specimen. δ_t was obtained from the three-point bending test (on the

non-precracked and non-indented beam), and δ_s was calculated from Timoshenko beam theory [22] using E and ν of the SLS glass,

$$\delta_s = \frac{2P}{EB} \left(\frac{S}{2W} \right)^2 \left\{ \frac{S}{2W} + \frac{1}{4} \left[2.85 \left(\frac{S}{2W} \right)^{-1} - 0.42 \left(\frac{S}{2W} \right)^{-2} \right] \right\}, \quad (5)$$

where P is the applied load, W is the specimen width (height, **Figure 1a**), B is the specimen breadth (smallest side, **Figure 1a**), and S is the span length of the three-point bending test (**Figure 1c**). **Figure 2** shows three curves of P - δ_s , P - δ_m and P - δ_t , where δ_s is calculated from Eq. (5) and $\delta_m = \delta_t - \delta_s$. In order to use the machine displacement for any applied load, we need to generalize the machine displacement as a function of applied load. From **Figure 2**, we find that the P - δ_m curve can be divided into two parts, i.e. the low load part is from 0 to 6 N and the high load part from 6 to ~17 N. As such, we plot two machine displacement-load curves as shown in **Figure 3**. To simplify the calculation, we used the polynomial function with the R-squared value better than 0.99 in both cases. We then obtained Eqs. (6) and (7) for $0.12 \text{ N} \leq P \leq 6 \text{ N}$ and $6 \text{ N} \leq P < 17 \text{ N}$, respectively.

$$\delta_m = -0.0001P^6 + 0.0026P^5 - 0.0286P^4 + 0.174P^3 - 0.6385P^2 + 1.6854P + 0.9879, \quad (6)$$

$$\delta_m = 0.0007P^3 - 0.0306P^2 + 0.7819P + 0.6693. \quad (7)$$

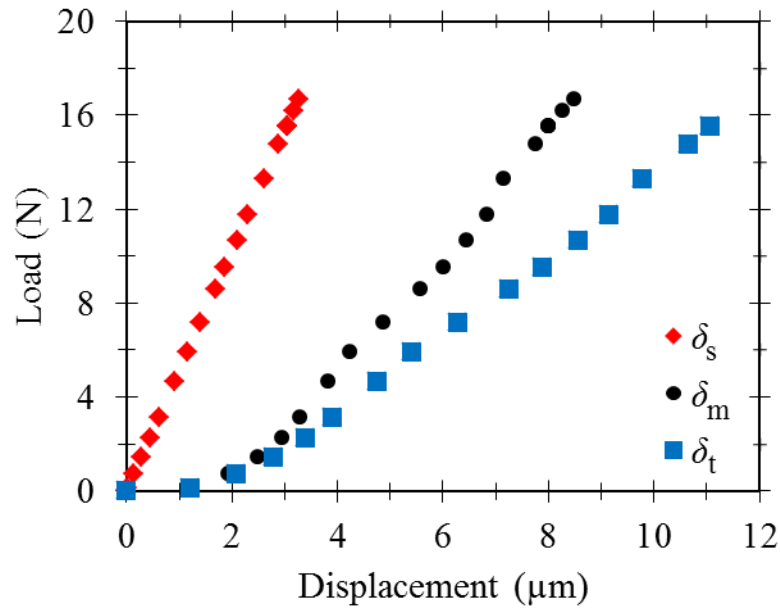


Figure 2: Load-displacement curves of the reference SLS specimen (red), the machine with three-point bending set-up (black), and as-experimented three-point bending (blue). The machine displacement (δ_m) was

calculated from the total displacement (δ_t) and the specimen deflection (δ_s) as $\delta_m = \delta_t - \delta_s$. The SLS specimen is a rectangular beam with a dimension of $B \times W \times L = 2.771 \times 3.831 \times 25.002$ mm³ and elastic moduli (E , ν) = (72 GPa, 0.231) as measured using ultrasonic echography technique. The span length (S) of the three-point bending is equal to 20 mm.

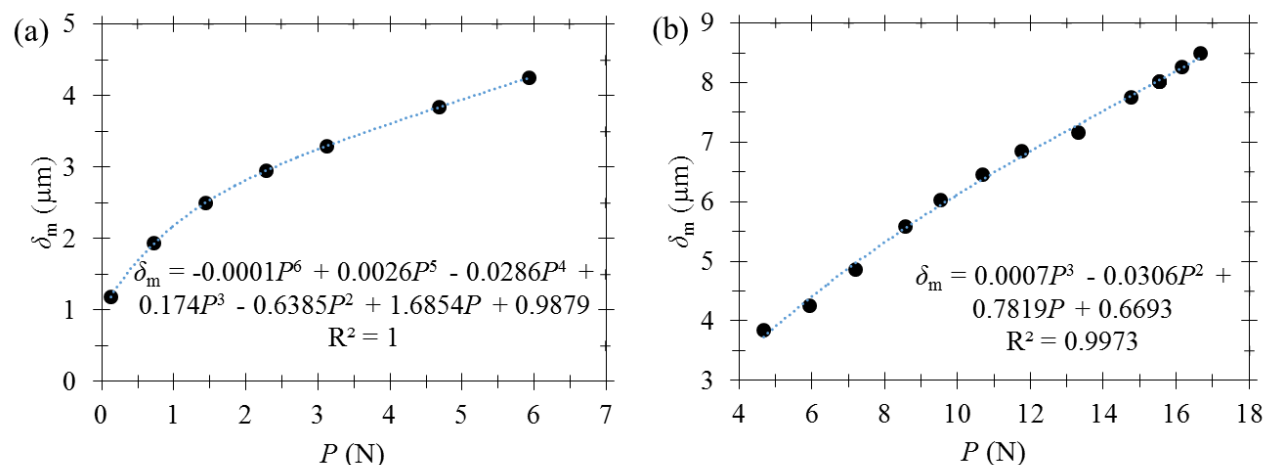


Figure 3: Machine displacement (δ_m) as a function of applied load (P). (a) For P from 0.12 N to 6 N. (b) For P from 5 N to 16.6 N. Blue dotted lines represent the polynomial curve fittings (see Eqs. (6) and (7)).

3. Results and discussion

3.1. Glass transition temperature, density, and elastic moduli

Glass transition temperature, density, and elastic moduli of the six studied glasses are shown in **Table 1**. T_g ranges from 428 to 670 °C. Barium-borate glasses have the lowest T_g , whereas aluminoborate glasses have the highest T_g . In the barium-borate glasses, the increase of Cs_2O from 15 mol% to 22.5% (by decreasing the BaO content) leads to the decrease of T_g by 30 °C, which is expected based on the weaker alkali-oxygen relative to alkaline earth-oxygen bonds. In the aluminoborate glasses, the 10 mol% replacement of Al_2O_3 by Ga_2O_3 does not effectively affect the T_g , presumably due to the similar structures roles of Al^{3+} and Ga^{3+} [23]. In the zinc-borate glasses, the replacement of Cs_2O (of 5 mol%) and B_2O_3 (of 2 mol%) by ZnO (of 5 mol%) and Ta_2O_5 (of 2 mol%) leads to the increase of T_g by 36 °C, which is likely due to an increase in average field strength of the oxides upon this replacement.

Table 1: Glass transition temperature (T_g), density (ρ), Shear modulus (G), Bulk modulus (B), Young's modulus (E), Poisson's ratio (ν), and fracture energy (G_c) of the six oxide glasses. Estimated errors for T_g , ρ , G , B , E , ν , and G_c do not exceed 2 °C, 0.01 g cm⁻³, 0.5 GPa, 0.6 GPa, 0.6 GPa, 0.005, and 0.5 J m⁻², respectively. ^a is the data taken from Ref. [17].

Glass code	T_g [°C]	ρ [g cm ⁻³]	G [GPa]	B [GPa]	E [GPa]	ν [-]	G_c [J m ⁻²]
20La30Al50B	670	3.79	40.0	89.7	104.4	0.306	6.301
20La20Al10Ga50B	669	4.07	38.7	85.3	100.8	0.303	6.980
15Cs30Ba55B	458	3.64	14.0	37.3	37.4	0.333	4.606
22.5Cs22.5Ba55B	428	3.59	12.4	30.7	32.8	0.322	3.532
5Cs50Zn45B	512	3.48	19.6	46.4	51.5	0.315	8.330
2Ta55Zn43B	548 ^a	4.04	31.1	85.1	83.7	0.336 ^a	9.001

Density ranges from 3.48 g cm⁻³ (for 5Cs50Zn45B) to 4.07 g cm⁻³ (for 20La20Al10Ga50B). The 10% replacement of Al₂O₃ by Ga₂O₃ in 20La30Al50B leads to the increase of the density by 7.4%. This increase is expected since amorphous gallium oxide (a-Ga₂O₃) has a density ($\rho(\text{a-Ga}_2\text{O}_3) = 5.3 \text{ g cm}^{-3}$) higher than that of the amorphous alumina (a-Al₂O₃, $\rho(\text{a-Al}_2\text{O}_3) = 3.255 \text{ g cm}^{-3}$) [8,24]. For the two cesium barium-borate glasses, their amorphous densities are not available. However, based on their crystalline densities, $\rho(\text{dry-Cs}_2\text{O}) = 4.65 \text{ g cm}^{-3} < \rho(\text{dry-BaO}) = 5.72 \text{ g cm}^{-3}$ [25], the density of 15Cs30Ba55B should be greater than that of 22.5Cs22.5Ba55B (**Table 1**). For the two zinc-borate glasses, we note that $\rho(\text{dry-B}_2\text{O}_3) = 2.46 \text{ g cm}^{-3} < \rho(\text{dry-Cs}_2\text{O}) = 4.65 \text{ g cm}^{-3} < \rho(\text{dry-ZnO}) = 5.61 \text{ g cm}^{-3} < \rho(\text{dry-Ta}_2\text{O}_5) = 8.2 \text{ g cm}^{-3}$ [25]. As such, the replacement of 5 mol% of Cs₂O by ZnO and 2 mol% of B₂O₃ by Ta₂O₅ leads to 16% increase of density in 2Ta55Zn43B comparing to that of 5Cs50Zn45B. In fact, the high density increase can simply be explained by the much higher (~4 times) density of amorphous Ta₂O₅ ($\rho(\text{a-Ta}_2\text{O}_5) = 6.8 \text{ g cm}^{-3}$ [26]) compared to that of amorphous B₂O₃ ($\rho(\text{a-B}_2\text{O}_3) = 1.85 \text{ g cm}^{-3}$ [27]).

G , B , E , and ν of the six studied glasses range from 12.4 to 40 GPa, 30.7 to 89.7 GPa, 32.8 to 104.4 GPa, and 0.303 to 0.336, respectively. G , B , and E have the similar trend and all increase with increasing T_g ,

This is the author's peer reviewed, accepted manuscript. However, the online version of record will be different from this version once it has been copyedited and typeset.
PLEASE CITE THIS ARTICLE AS DOI: 10.1063/1.50096855

whereas ν does not show any clear relation with T_g (**Figure 4**). The similar trend of G , B , and E and its relationship with T_g can be explained by the fact that all the four parameters scale with molar dissociation energy of the glass chemical compositions [28]. To simplify, we would only discuss the trend of Young's modulus of these six studied glasses. The molar bond energy of La-O ($\sim 798 \text{ kJ mol}^{-1}$) is much higher than that of Cs-O ($\sim 293 \text{ kJ mol}^{-1}$) and Zn-O ($\sim 250 \text{ kJ mol}^{-1}$), and the molar bond energy of Al-O ($\sim 502 \text{ kJ mol}^{-1}$) is similar to that of Ba-O ($\sim 562 \text{ kJ mol}^{-1}$), explaining the higher E of lanthanum aluminoborate glasses compared to the other four studied glasses [29]. Moreover, the slightly higher E of 20La30Al50B than that of 20La20Al10Ga50B can be directly explained by the higher molar-diatomic bond energy of Al-O than Ga-O ($\sim 374 \text{ kJ mol}^{-1}$). Similarly, $E(15\text{Cs}30\text{Ba}55\text{B}) > E(22.5\text{Cs}22.5\text{Ba}55\text{B})$ can be directly explained by the higher bond energy of Ba-O compared to that of Cs-O. However, the much higher E of 2Ta55Zn43B than that of 5Cs50Zn45B can likely be explained by (i) the higher bond energy of Ta-O ($\sim 839 \text{ kJ mol}^{-1}$) than that of B-O ($\sim 809 \text{ kJ mol}^{-1}$) and (ii) the much higher density of 2Ta55Zn43B than that of 5Cs50Zn45B. For the higher E of zinc-borate glasses relative to barium-borate glasses, we need to recount that once the mol% of modifiers (e.g. Cs₂O, BaO) is higher than half of that of the glass former (e.g. B₂O₃), their bond energy in diatomic cations should be used instead [27]; in our case, the bond energy in diatomic cation of Zn⁺-O ($\sim 161 \text{ kJ mol}^{-1}$) is much higher than that of Cs⁺-O ($\sim 59 \text{ kJ mol}^{-1}$).

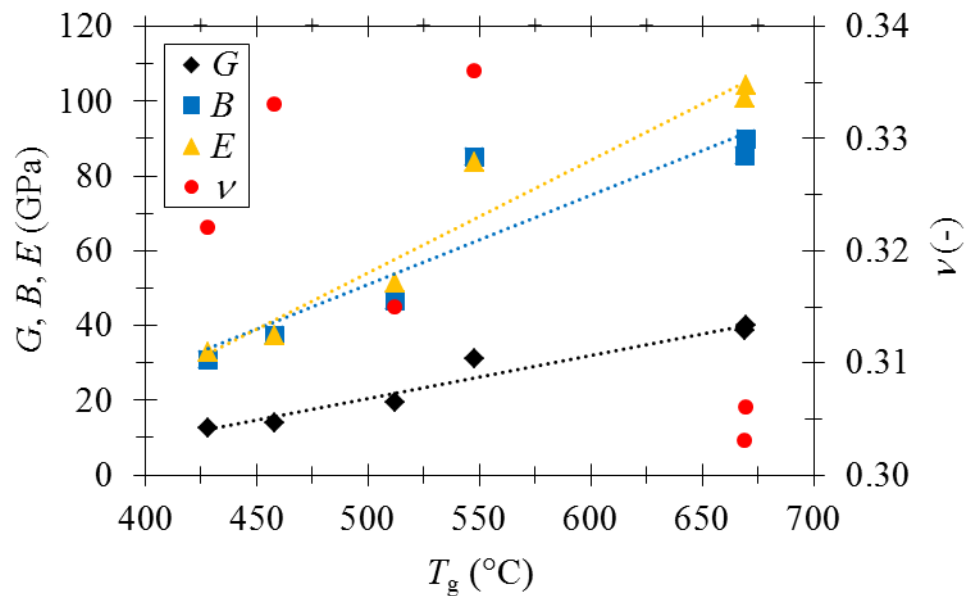


Figure 4: Relationship between elastic properties (G , B , E , ν) and glass transition temperature (T_g) of the six studied glasses. The dotted lines are guidelines to the eyes.

3.2. Fracture energy

Figure 5 shows the load-displacement curves of the three-point bending test in the fracture step of the SEPB method for both δ_t and δ_s of a 20La20Al10Ga50B specimen. From these curves, we could calculate the work of fracture ($wof = \int Pd\delta$). The wof calculated using δ_t ($wof(\delta_t) = 12.561 \text{ N } \mu\text{m}$) is greater than that calculated using δ_s ($wof(\delta_s) = 11.473 \text{ N } \mu\text{m}$). It is noteworthy that the $wof(\delta_t)$ consists of the work to fracture the specimen with a fracture surface (A) and the work to deform the machine ($wof(\delta_m)$). With the same value of A of 1.725 mm^2 , we could calculate the fracture energy of 20La20Al10Ga50B specimen ($G_C(\delta_s)$) to be 6.652 J m^{-2} and that of specimen together with the machine ($G_C(\delta_t)$) to be 7.282 J m^{-2} . This difference shows the importance of determining the real deflection of the specimen to calculate the glass fracture energy from the work of fracture.

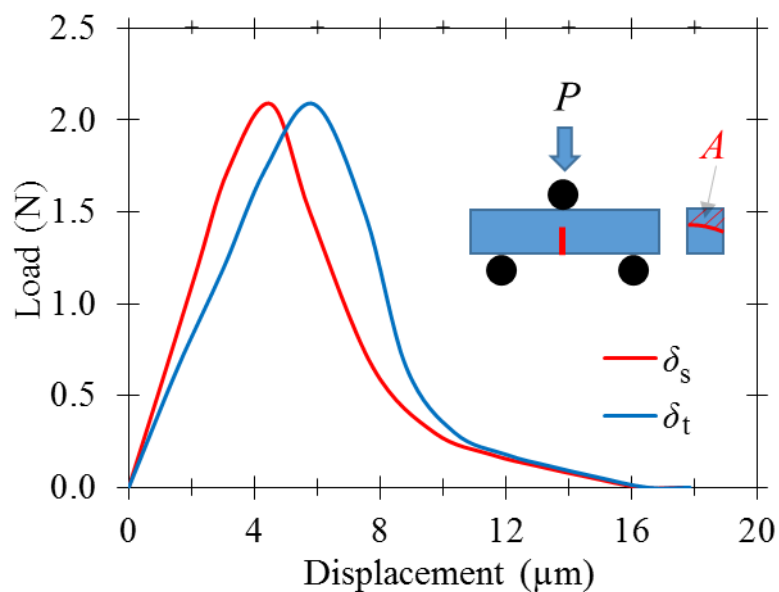


Figure 5: Load-displacement curves of the three-point bending (fracture step) for the total displacement (δ_t , blue) and for the specimen deflection (δ_s , red) of a 20La20Al10Ga50B specimen. P and A represent the applied load and fracture surface, respectively.

The average fracture energy of the six studied glasses, calculated from both total displacement and specimen deflection, is shown in **Table 2**. In general, $G_C(\delta_t)$ is greater than $G_C(\delta_s)$, with differences from 5.7% (for 5Cs50Zn45B) to 12.7% (for 22.5Cs22.5Ba55B). These differences indicate the non-linearity of the machine displacement during bending and the importance of the displacement calibration by using Eqs. (6) and (7) to determine the machine displacement. $G_C(\delta_s)$ of the six studied glasses ranges from 3.532 J m⁻² for 22.5Cs22.5Ba55B to 9.001 J m⁻² for 2Ta55Zn43B. We note that among the three glass families, the barium-borate has the lowest $G_C(\delta_s)$, whereas the zinc-borate has the highest $G_C(\delta_s)$. To explain this trend, we need the knowledge of the fracture energy and that of the modifier-former relation in a glass system.

Table 2: Fracture energy calculated from total displacement ($G_C(\delta_t)$) and from specimen deflection ($G_C(\delta_s)$) of the six studied glasses. Each value was averaged from at least three experiments, and the error is better than 0.350 J m⁻² for both cases.

Glass code	20La30Al 50B	20La20Al10Ga 50B	15Cs30Ba 55B	22.5Cs22.5Ba 55B	5Cs50Zn 45B	2Ta55Zn 43B
$G_C(\delta_t)$ [J m ⁻²]	6.772	7.412	5.030	3.982	8.802	9.611
$G_C(\delta_s)$ [J m ⁻²]	6.301	6.980	4.606	3.532	8.330	9.001

First, the two main parameters that define the fracture energy are glass density and molar diatomic bond energy [27]. In the La-alumino/gallioborate glasses, the 10 mol% replacement of Al₂O₃ by Ga₂O₃ leads to the ~11% increase in G_C . Although the bond energy of Ga-O is smaller than that of Al-O (as discussed in Section 3.1), 20La20Al10Ga50B has 7.5% greater density than that of 20La30Al50B. In the barium-borate glasses, the bond energy of Cs-O is about half the value of that of Al-O (see Section 3.1) and the density of 22.5Cs22.5Ba55B is slightly smaller than that of 15Cs30Ba55B (Table 1). As such, the 7.5 mol% replacement of BaO by Cs₂O leads to the 23% decrease in G_C . In the zinc-borate glasses, the bond energy of Zn-O is slightly lower than that of Cs-O, but the bond energy of Ta-O is higher than that of B-O (Section 3.1) and the density of 2Ta55Zn43B is 16% higher than that of 5Cs50Zn45B (Table 1). This explains the 8% increase in fracture energy of 2Ta55Zn43B compared to 5Cs50Zn45B.

Comparing the fracture energy among the three glass families, it is straightforward to explain the higher fracture energy of alumino/gallio-borate relative to barium-borate glasses since both density and bond energy is much higher in the former than in the latter glasses. However, this molar bond energy and density differences cannot fully explain the fact that the zinc-borate glasses feature the highest fracture energy. To explain this, it is noted that B_2O_3 is the glass network former, while Al_2O_3 , Ga_2O_3 , La_2O_3 , Ta_2O_5 and ZnO can act as either modifier or former in the system, while Cs_2O and BaO act as pure modifiers [16,27,30]. The presence of pure modifiers leads to the increase of non-bridging oxygen, creating easy paths for the crack to propagate without breaking the glass former bonds [27]. However, if we compare monovalent (Cs_2O in this study) to divalent oxides (BaO and ZnO in this study), the former needs two oxygen atoms, whereas the latter need only one to stabilize the system. As such, the divalent cations tend to promote higher fracture energy. For example, the 22.5Cs22.5Ba55B glass, which contains 22.5 mol% of Cs_2O , has the lowest fracture energy among the six studied glasses, and 23% lower fracture energy compared to 15Cs22.5Ba55B. Unlike the barium-borate glasses, the zinc-borate glass contains only 5 mol% of the monovalent oxide (i.e., Cs_2O), leading to the need of breaking all the bonds in the glass system during fracture. Moreover, the Zn atom has the molar mass ($M_0(Zn) = 65.4 \text{ g mol}^{-1}$) that is less than half the value of Cs atom ($M_0(Cs) = 132.9 \text{ g mol}^{-1}$) and Ba atom ($M_0(Ba) = 137.3 \text{ g mol}^{-1}$). This small molar mass of Zn, together with the comparable density of this glass to the others, causes the zinc-borate glass to have a small molar volume so that it needs to break nearly every bond in the chemical system in order to fracture the glass. As such, the fracture energy of the zinc-borate is high.

3.3. Correlating fracture energy with elastic properties

Figure 6 shows the fracture energy as a function of elastic properties for the six studied glasses. While there is no clear relation between the Poisson's ratio and fracture energy in the studied glasses, there appear to be a non-linear relationship between fracture energy and the three elastic moduli (G , B and E). The data show that the high Young's (shear or bulk) modulus does not guarantee the high fracture energy. In fact, the high E may lead to lower fracture energy. The explanation to this finding is that G_C decreases with increasing E as seen in the Irwin's similarity principle [31], $G_C = K_{Ic}^2(E')^{-1}$, where $E' = E$ in the case of plane stress and $E' = E(1-\nu)$ in the case of plane strain. In the present, we have the plane strain condition because we used the

SEPB method and our specimen beam is thick ($B/W > 0.5$) [21]. The equation by Irwin shows that for two materials with the same fracture toughness, the one with the higher Young's modulus would give rise to lower fracture energy than that with lower Young's modulus. This means that the glasses with the E of 51.5 and 83.7 GPa, which are the zinc-borate glasses (see **Table 1**, **Table 2** and **Figure 6**), are the most ductile ones among the studied glasses. We note here that a *ductile* glass possesses the ability to deform before fracture corresponding to high fracture-energy glass, whereas a glass with high fracture toughness is referred to as *tough* [12,32]. Next, we will further consider the relation between fracture energy and the two elastic properties (E and ν) by comparing our findings to the literature results.

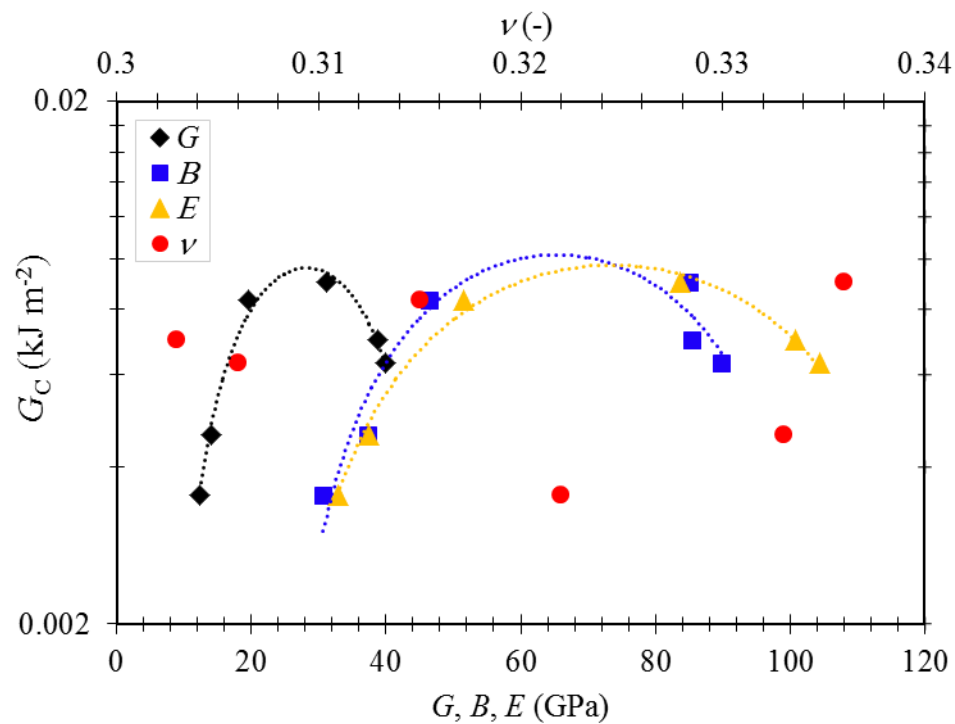


Figure 6: Fracture energy (G_c) as a function of elastic moduli (G , B , E and ν) for the six studied glasses. The black, blue and yellow dotted lines are a guide for the eye for G , B and E , respectively.

Figure 7 shows the dependence of fracture energy on Poisson's ratio for a range of materials, including the six studied glasses. It shows the brittle-to-ductile (BTD) transition $\nu_{\text{BTD}} = 0.32$ as discussed previously, with various non-crystalline solids and most metallic glasses having $\nu > 0.32$ and exhibiting a ductile fracture behavior (the data on the right-hand side of the BTD transition in **Figure 7**). Although three

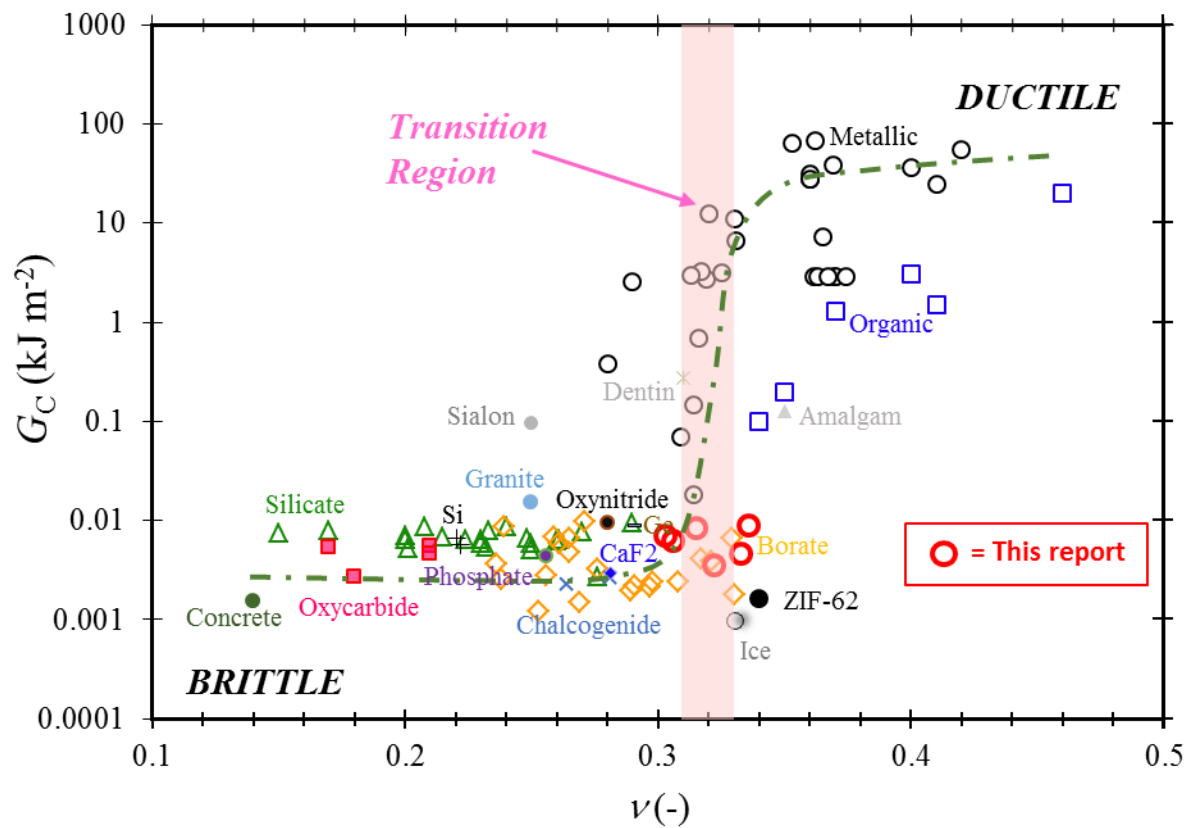


Figure 7: Fracture energy (G_C) as a function of Poisson's ratio (ν) for various materials, showing a brittle-to-ductile transition in the range of ν between 0.31 and 0.33. The figure is reproduced with the data from Refs. [12,33], and extended with data from Refs. [3,10,21,27,32,34–37]. The error of G_C and ν is estimated to be 15% and 0.005, respectively. The green dashed line is a guide for the eye.

When different types of glasses are plotted together, the relationship between the fracture energy and Young's modulus seems to exhibit a positive, linear relation in the case of oxide glasses and a non-

monotonic relation in the case of metallic glasses (**Figure 8**). A similar trend is found for the relationship between G_C and $E/(1-\nu^2)$ (Figure S1). This shows that high fracture energy alone cannot assure the presence of ductility in a glass. As such, we need to check whether the high fracture energy is caused by the high elastic moduli or not. For example, the metallic glasses in blocks II and III (the right wing side of the black dotted line) in **Figure 8** are those in the BTB transition or brittle region, whereas those in block I (the left wing side) are the glasses in the ductile region in **Figure 7**. The metallic glasses in block IV have the same fracture energy as those in block III (see Figures 8 and S1) but lower E (~ 50 GPa for IV and ~ 200 GPa for III), suggesting that the glasses in block IV should be in the ductile or BTB regions rather than in the brittle region. This is another evidence that a ductile glass is the one with high fracture energy, but with relatively low Young's modulus.

We should note that the light blue arrow in Figures 8 and S1 is used to guide the eye to the possible tendency of the brittle fracture when all the glass types are plotted together. However, if we consider only a glass type such as phosphate glasses, for glasses with the same E value of 50 GPa in Figure 8, the phosphate glasses has the lowest G_C of ~ 0.002 kJ m $^{-2}$ and the highest G_C of ~ 0.02 kJ m $^{-2}$ (about 10 times higher). This raises the question whether there is any ductility in the phosphate glasses and whether it makes sense to plot all the fracture energy data in one figure. While the question needs more investigation, the results shown in Figure 8 highlight that a glass with low G_C with high E' is brittle (e.g., block III for metallic glass), a glass with high G_C and low E' is ductile (e.g., block I for metallic glass), and a glass with relatively high G_C and low E' is a glass in the BTB region (e.g., block II for metallic glass).

Finally, we should note that the use of Poisson's ratio as a predictor of fracture toughness of glasses has been questioned from a theoretical point of view [38], in agreement the experimental findings of this work. Namely, that the effect of Poisson's ratio is extrinsic, mediated through the deformation geometry. Instead of Poisson's ratio, it is proposed that the two parameters A_g (related to glassy disorder) and χ (related to elastic heterogeneity) can control and predict the damage tolerance of glasses [38]. Specifically, the ratio A_g/χ may predict an intrinsic transition from a damage-tolerant, ductile-like response to a catastrophic failure, brittle-like response [2].

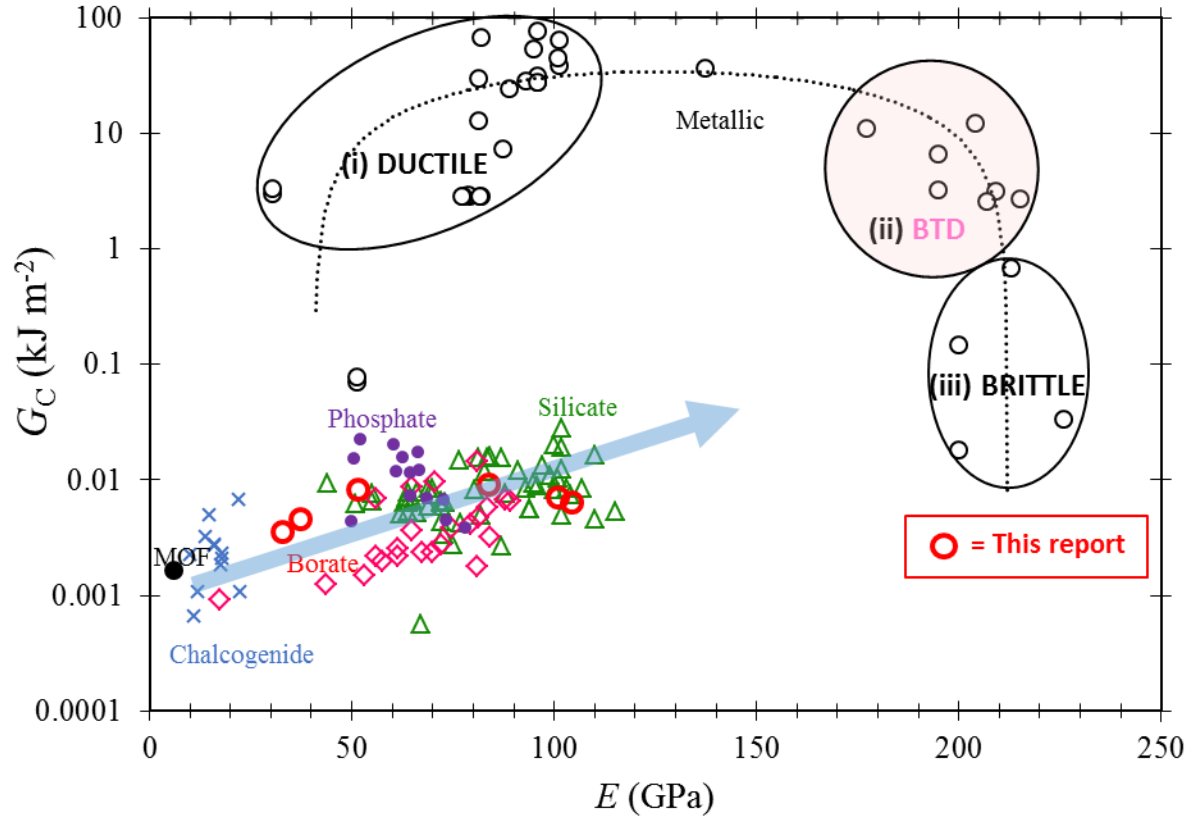


Figure 8: Fracture energy (G_C) as a function of Young's modulus (E) for various glasses. The data was taken from Refs. [3,10,12,21,27,32,34–37]. The transparent, light blue arrow line is guide for the eye and represents the possible relationship between G_C and E . The black dotted line is a guide for the eye in the case of metallic glasses and represents the non-linear relationship between G_C and E similar to that shown in **Figure 6**.

4. Conclusion

We have studied the fracture energy of six oxide glasses with high Poisson's ratio from 0.30 to 0.34. First of all, we have found that it is mandatory to calibrate the machine displacement to determine the real glass specimen deflection in order to avoid overestimating the fracture energy. Although it is suggested in the literature that glasses with Poisson's ratio higher than 0.32 are ductile, we found no clear relation between ductility and Poisson's ratio in the case of oxide glasses, even for those with Poisson's ratio above this limit. This suggests that Poisson's ratio is not the only factor to tailor the ductility of oxide glasses. Besides, we have found a positive relation between the fracture energy and Young's modulus of oxide glasses as well as some metallic glasses. This relation can be used to explain the absence of ductility in the glasses. The

metallic glasses with lower Young's modulus could possess the same fracture energy relative to those with higher Young's modulus because there is a presence of ductility during fracturing. In future work, it would thus be interesting to explore glasses, for which fracture toughness is maximized but moduli is minimized to verify if the fracture energy becomes maximized.

Supplemental Material

See supplementary material for the relationship between G_C and $E/(1-\nu^2)$ for various glasses.

Acknowledgements

This work was supported by Independent Research Fund Denmark (0136-00011B).

References

- [1] T. Rouxel and S. Yoshida, *The Fracture Toughness of Inorganic Glasses*, J. Am. Ceram. Soc. **100**, 4374 (2017).
- [2] L. Wondraczek, E. Bouchbinder, A. Ehrlicher, J. C. Mauro, R. Sajzew, and M. M. Smedskjaer, *Advancing the Mechanical Performance of Glasses: Perspectives and Challenges*, Adv. Mater. 2109029 (2022).
- [3] T. To, Fracture Toughness and Fracture Surface of Inorganic and Non-Metallic Glasses, Université de Rennes 1 (PhD thesis), 2019.
- [4] S. Karlsson, B. Jonson, and C. Stålhandske, *The Technology of Chemical Glass Strengthening - A Review*, Glas. Technol. Eur. J. Glas. Sci. Technol. Part A **51**, 41 (2010).
- [5] B. Wang, Y. Yu, M. Wang, J. C. Mauro, and M. Bauchy, *Nanoductility in Silicate Glasses Is Driven by Topological Heterogeneity*, Phys. Rev. B **93**, 064202 (2016).
- [6] K. Zheng, C. Wang, Y. Q. Cheng, Y. Yue, X. Han, Z. Zhang, Z. Shan, S. X. Mao, M. Ye, Y. Yin, and E. Ma, *Electron-Beam-Assisted Superplastic Shaping of Nanoscale Amorphous Silica*, Nat. Commun. **1**, 24 (2010).
- [7] J. Luo, J. Wang, E. Bitzek, J. Y. Huang, H. Zheng, L. Tong, Q. Yang, J. Li, and S. X. Mao, *Size-Dependent Brittle-to-Ductile Transition in Silica Glass Nanofibers*, Nano Lett. **16**, 105 (2016).

This is the author's peer reviewed, accepted manuscript. However, the online version of record will be different from this version once it has been copyedited and typeset.
PLEASE CITE THIS ARTICLE AS DOI: 10.1063/1.50096855

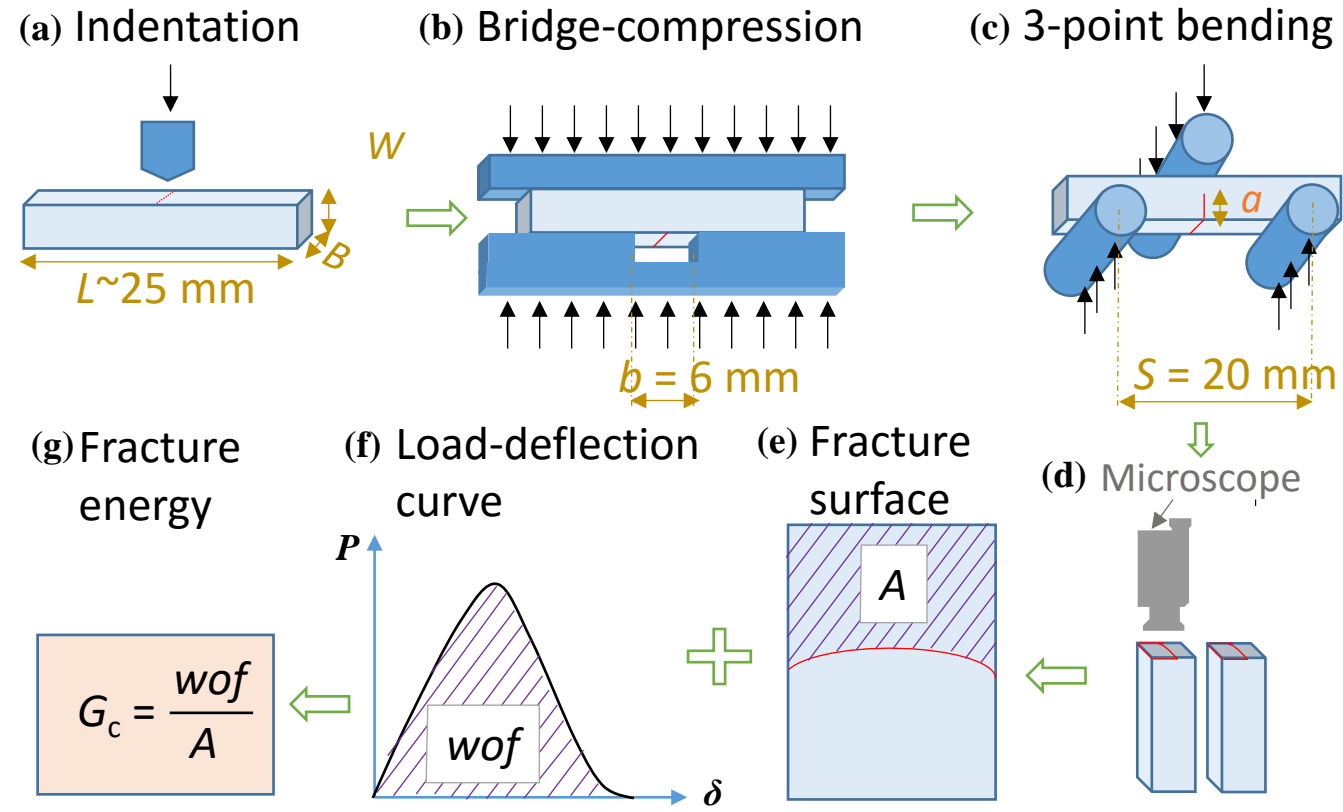
- [8] E. J. Frankberg, J. Kalikka, F. G. Ferré, L. Joly-Pottuz, T. Salminen, J. Hintikka, M. Hokka, S. Koneti, T. Douillard, B. Le Saint, P. Kreiml, M. J. Cordill, T. Epicier, D. Stauffer, M. Vanazzi, L. Roiban, J. Akola, F. Di Fonzo, E. Levänen, and K. Masenelli-Varlot, *Highly Ductile Amorphous Oxide at Room Temperature and High Strain Rate*, *Science* (80-.). **366**, 864 (2019).
- [9] K. Januchta, M. Stepniewska, L. R. Jensen, Y. Zhang, M. A. J. Somers, M. Bauchy, Y. Yue, and M. M. Smedskjaer, *Breaking the Limit of Micro-Ductility in Oxide Glasses*, *Adv. Sci.* **6**, 1901281 (2019).
- [10] T. To, S. S. Sørensen, J. F. S. Christensen, R. Christensen, L. R. Jensen, M. Bockowski, M. Bauchy, and M. M. Smedskjaer, *Bond Switching in Densified Oxide Glass Enables Record-High Fracture Toughness*, *ACS Appl. Mater. Interfaces* **13**, 17753 (2021).
- [11] S. F. Pugh, *Relations between the Elastic Moduli and the Plastic Properties of Polycrystalline Pure Metals*, *Philos. Mag.* **45**, 823 (1954).
- [12] J. J. Lewandowski, W. H. Wang, and A. L. Greer, *Intrinsic Plasticity or Brittleness of Metallic Glasses*, *Philos. Mag. Lett.* **85**, 77 (2005).
- [13] G. N. Greaves, A. L. Greer, R. S. Lakes, and T. Rouxel, *Poisson's Ratio and Modern Materials*, *Nat. Mater.* **10**, 823 (2011).
- [14] G. B. Rouse, E. I. Kamitsos, and W. M. Risen, *Brillouin Spectra of Mixed Alkali Glasses: $XC_s_2O(1-x)Na_2O5SiO_2$* , *J. Non. Cryst. Solids* **45**, 257 (1981).
- [15] G. Srinivasarao and N. Veeraiiah, *Characterization and Physical Properties of $PbO-As_2O_3$ Glasses Containing Molybdenum Ions*, *J. Solid State Chem.* **166**, 104 (2002).
- [16] K. Januchta, R. Sun, L. Huang, M. Bockowski, S. J. Rzoska, L. R. Jensen, and M. M. Smedskjaer, *Deformation and Cracking Behavior of La_2O_3 -Doped Oxide Glasses with High Poisson's Ratio*, *J. Non. Cryst. Solids* **494**, 86 (2018).
- [17] M. B. Østergaard, S. R. Hansen, K. Januchta, T. To, S. J. Rzoska, M. Bockowski, M. Bauchy, and M. M. Smedskjaer, *Revisiting the Dependence of Poisson's Ratio on Liquid Fragility and Atomic Packing Density in Oxide Glasses*, *Materials (Basel)*. **12**, 2439 (2019).
- [18] M. Kodama and S. Kojima, *Velocity of Sound in and Elastic Properties of Alkali Metal Borate Glasses*, *Phys. Chem. Glas. J. Glas. Sci. Technol. Part B* **55**, 1 (2014).
- [19] A. Makishima and J. D. Mackenzie, *Calculation of Bulk Modulus, Shear Modulus, and Poisson's*

- Ratio of Glass*, J. Non. Cryst. Solids **17**, 147 (1975).
- [20] J.-P. Poirier, *Introduction to the Physics of the Earth's Interior* (Cambridge University Press, 2000).
- [21] T. To, F. Célarié, C. Roux-Langlois, A. Bazin, Y. Gueguen, H. Orain, M. Le Fur, V. Burgaud, and T. Rouxel, *Fracture Toughness, Fracture Energy and Slow Crack Growth of Glass as Investigated by the Single-Edge Precracked Beam (SEPB) and Chevron-Notched Beam (CNB) Methods*, Acta Mater. **146**, 1 (2018).
- [22] S. P. Timoshenko and S. Woinowsky-Krieger, *Theory of Plate and Shells* (McGraw-Hill, New-York, 1959).
- [23] S. Sakka, H. Kozuka, K. Fukumi, and F. Miyaji, *Structures of Gallate, Aluminate and Titanate Glasses*, J. Non. Cryst. Solids **123**, 176 (1990).
- [24] D. Sun, Y. Gao, J. Xue, and J. Zhao, *Matching Vacancy Formation Energy and Defect Levels with the Density of Amorphous Ga₂O₃*, J. Mater. Sci. **55**, 9343 (2020).
- [25] D. R. Lide, *CRC Handbook of Chemistry and Physics*, Vol. 85 (CRC press, 2004).
- [26] Y. Guo and J. Robertson, *Comparison of Oxygen Vacancy Defects in Crystalline and Amorphous Ta₂O₅*, Microelectron. Eng. **147**, 254 (2015).
- [27] T. Rouxel, *Fracture Surface Energy and Toughness of Inorganic Glasses*, Scr. Mater. **137**, 109 (2017).
- [28] T. Rouxel, J.-I. Jang, and U. Ramamurty, *Indentation of Glasses*, Prog. Mater. Sci. **121**, 100834 (2021).
- [29] Y.-R. Luo, *Handbook of Bond Dissociation Energies in Organic Compounds* (CRC press, Boca Raton, 2002).
- [30] K. Januchta, R. E. Youngman, L. R. Jensen, and M. M. Smedskjaer, *Mechanical Property Optimization of a Zinc Borate Glass by Lanthanum Doping*, J. Non. Cryst. Solids (2019).
- [31] G. R. Irwin, *Analysis of Stresses and Strains Near the End of a Crack Traversing a Plate*, J. Appl. Mech. **24**, 361 (1957).
- [32] T. To, L. R. Jensen, and M. M. Smedskjaer, *On the Relation between Fracture Toughness and Crack Resistance in Oxide Glasses*, J. Non. Cryst. Solids **534**, 119946 (2020).
- [33] K. V Tian, B. Yang, Y. Yue, D. T. Bowron, J. Mayers, R. S. Donnan, C. Dobó-Nagy, J. W.

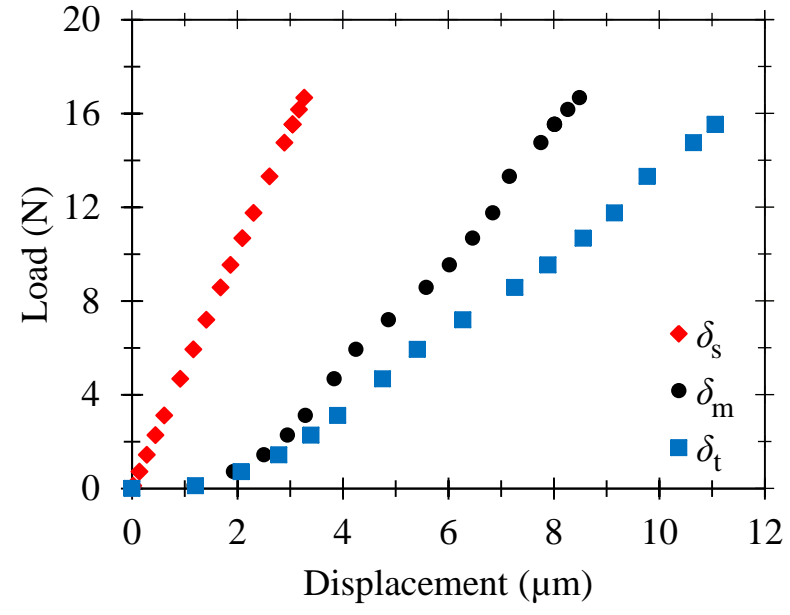
This is the author's peer reviewed, accepted manuscript. However, the online version of record will be different from this version once it has been copyedited and typeset.
PLEASE CITE THIS ARTICLE AS DOI: 10.1063/5.0096855

- Nicholson, D.-C. Fang, A. L. Greer, G. A. Chass, G. N. Greaves, and others, *Atomic and Vibrational Origins of Mechanical Toughness in Bioactive Cement during Setting*, *Nat. Commun.* **6**, 1 (2015).
- [34] K. Januchta, T. To, M. S. Bødker, T. Rouxel, and M. M. Smedskjaer, *Elasticity, Hardness, and Fracture Toughness of Sodium Aluminoborosilicate Glasses*, *J. Am. Ceram. Soc.* **102**, 4520 (2019).
- [35] T. To, S. S. Sørensen, M. Stepniewska, A. Qiao, L. R. Jensen, M. Bauchy, Y. Yue, and M. M. Smedskjaer, *Fracture Toughness of a Metal–Organic Framework Glass*, *Nat. Commun.* **11**, 2593 (2020).
- [36] T. To, F. Célarié, Y. Gueguen, N. G. Brou, C. Lim, R. Horm, V. Burgaud, M. Le Fur, J. Chollet, H. Orain, and T. Rouxel, *Environment Dependence of K_{Ic} of Glass*, *J. Non. Cryst. Solids* **566**, 120873 (2021).
- [37] T. To, C. Stabler, E. Ionescu, R. Riedel, F. Célarié, and T. Rouxel, *Elastic Properties and Fracture Toughness of SiOC-Based Glass-Ceramic Nanocomposites*, *J. Am. Ceram. Soc.* **103**, 491 (2020).
- [38] D. Richard, E. Lerner, and E. Bouchbinder, *Brittle to Ductile Transitions in Glasses: Roles of Soft Defects and Loading Geometry*, *MRS Bull.* **46**, 902 (2021).

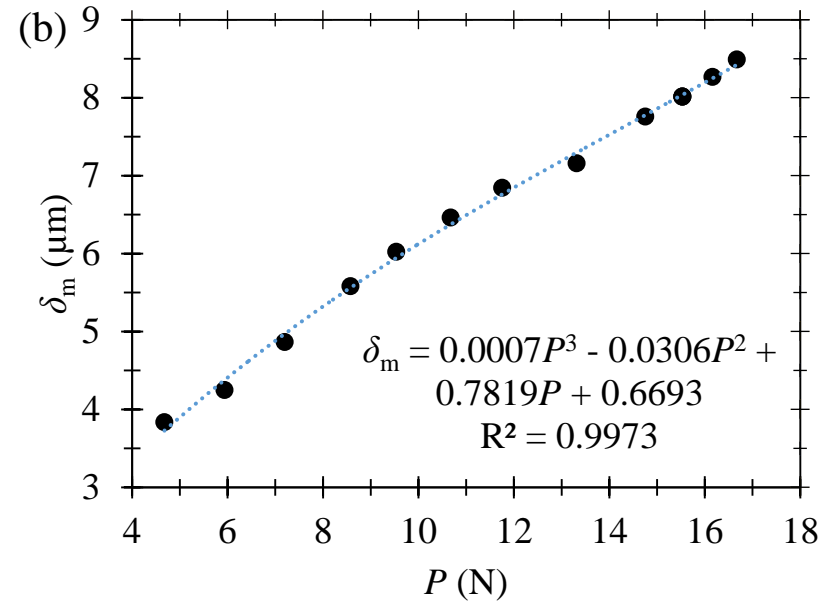
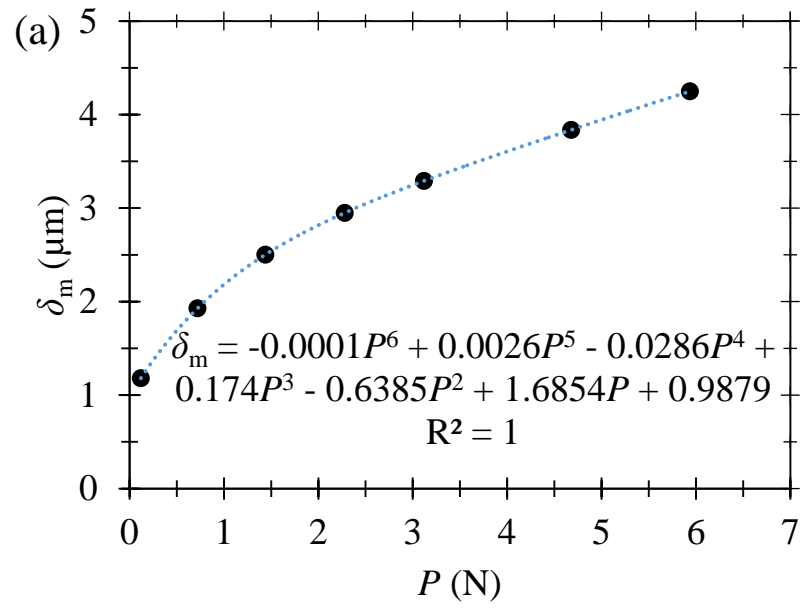
This is the author's peer reviewed, accepted manuscript. However, the online version of record will be different from this version once it has been copyedited and typeset.
 PLEASE CITE THIS ARTICLE AS DOI: 10.1063/5.0096855



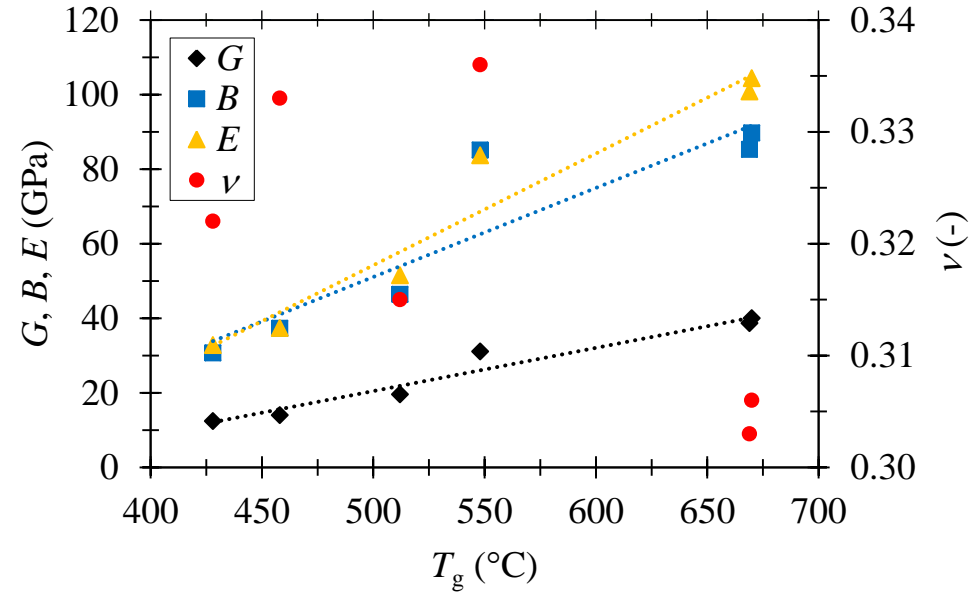
This is the author's peer reviewed, accepted manuscript. However, the online version of record will be different from this version once it has been copyedited and typeset.
PLEASE CITE THIS ARTICLE AS DOI: 10.1063/5.0096855



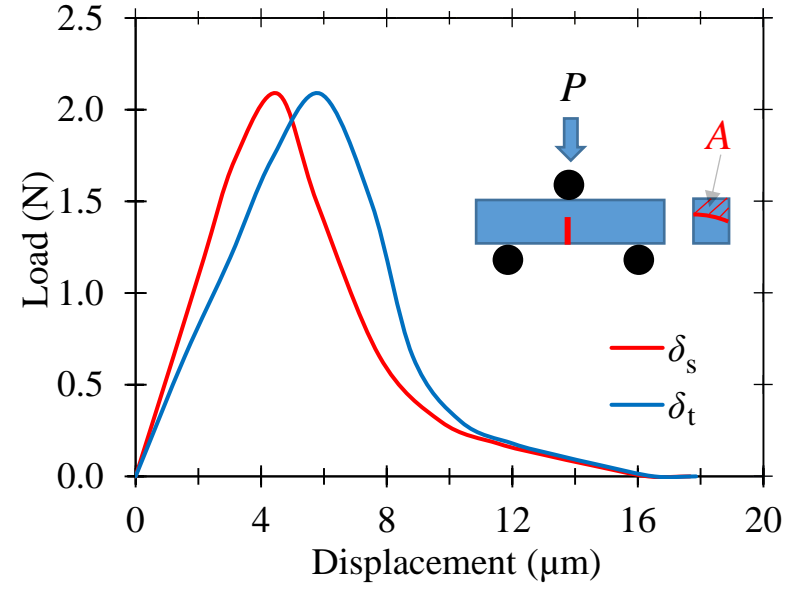
This is the author's peer reviewed, accepted manuscript. However, the online version of record will be different from this version once it has been copyedited and typeset.
PLEASE CITE THIS ARTICLE AS DOI: 10.1063/5.0096855



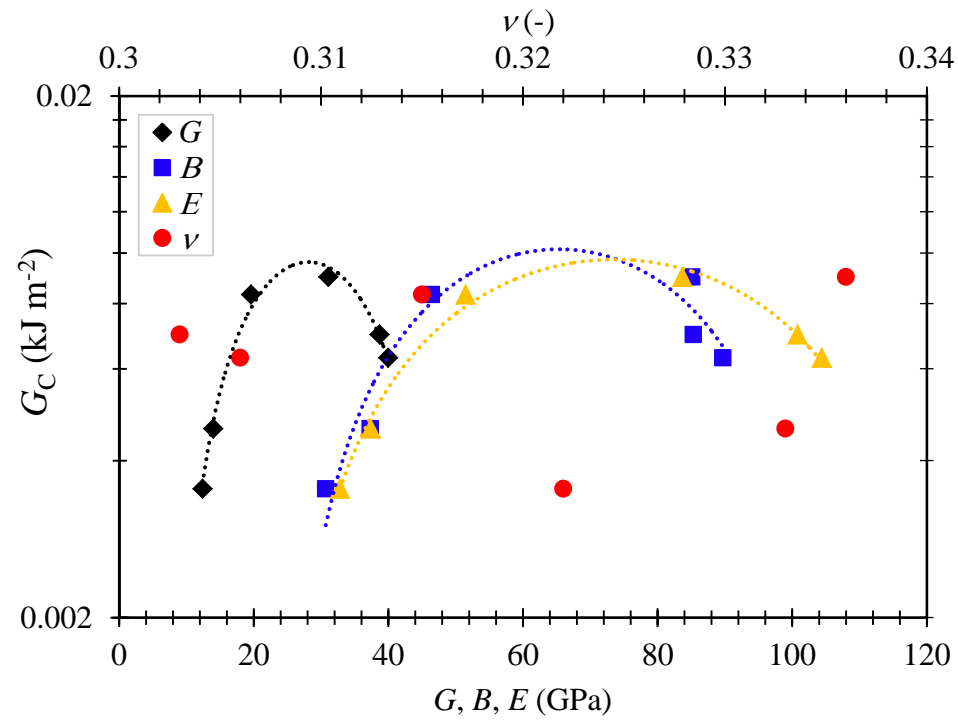
This is the author's peer reviewed, accepted manuscript. However, the online version of record will be different from this version once it has been copyedited and typeset.
PLEASE CITE THIS ARTICLE AS DOI: 10.1063/5.0096855



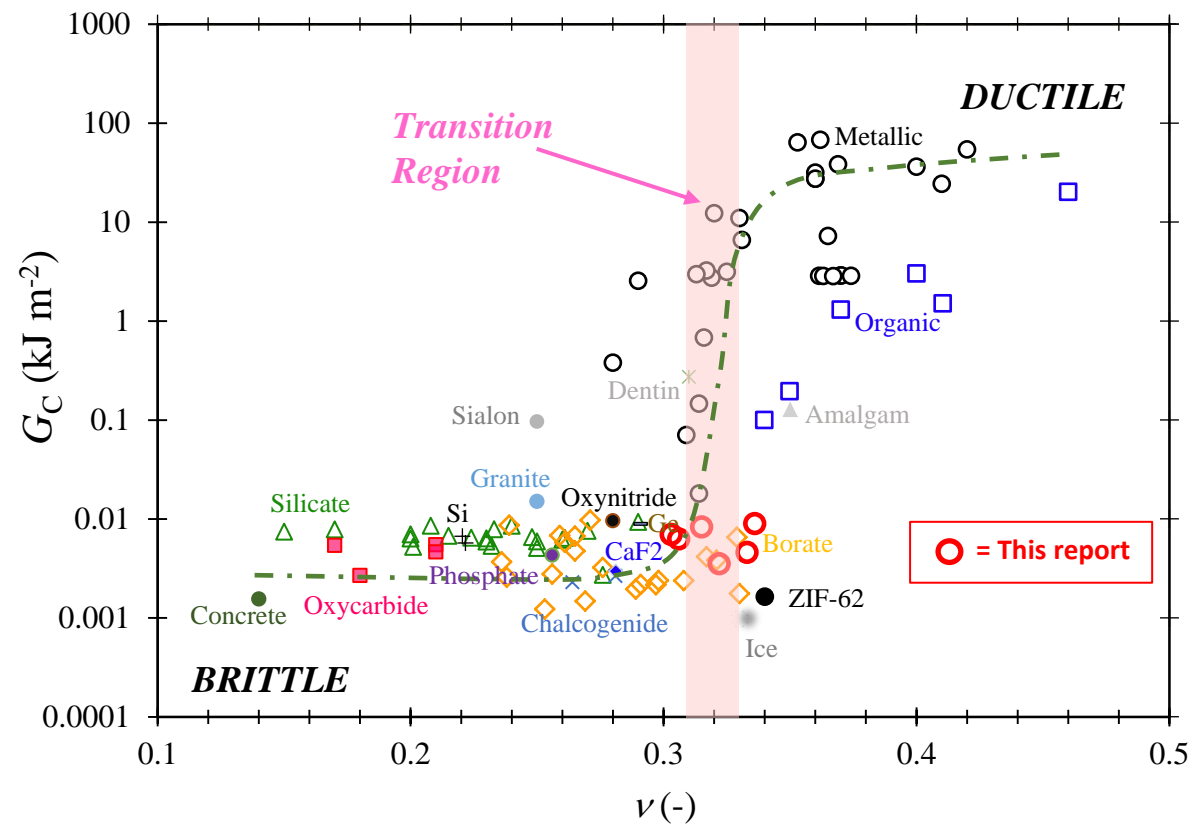
This is the author's peer reviewed, accepted manuscript. However, the online version of record will be different from this version once it has been copyedited and typeset.
PLEASE CITE THIS ARTICLE AS DOI: 10.1063/5.0096855



This is the author's peer reviewed, accepted manuscript. However, the online version of record will be different from this version once it has been copyedited and typeset.
PLEASE CITE THIS ARTICLE AS DOI: 10.1063/5.0096855



This is the author's peer reviewed, accepted manuscript. However, the online version of record will be different from this version once it has been copyedited and typeset.
PLEASE CITE THIS ARTICLE AS DOI: 10.1063/5.0096855



This is the author's peer reviewed, accepted manuscript. However, the online version of record will be different from this version once it has been copyedited and typeset.
PLEASE CITE THIS ARTICLE AS DOI: 10.1063/5.0096855

